South America Intraseasonal Precipitation: A Normal-Mode Approach

Victor C. Mayta[1,2*], André Seiji Wakate Teruya [2], Breno Raphaldini [2], Pedro L. Silva Dias [2], and Camila Sapucci [2].

[1]Department of Climate and Space Science and Engineering, University of Michigan, Ann Arbor, Michigan
[2]Departamento de Ciências Atmosféricas, IAG, Universidade de São Paulo, São Paulo, SP, Brasil

Key Points:

- Extratropical Rossby waves play an important role in the South American intraseasonal rainfall variability, mainly during the dry season
- Normal-mode decomposition of the South American intraseasonal variability shows that the SESA-SACZ pattern is dominated by rotational modes
- The normal-mode decomposition provides a powerful tool for diagnosing circulation model issues in order to improve rainfall prediction

*Climate and Space Research Building University of Michigan, 2455 Hayward St., Ann Arbor.

Corresponding author: Victor C. Mayta, vchavezmayta@gmail.com

Abstract

An alternative approach to assess the South America intraseasonal variability is presented. In this study, we use a normal-mode decomposition method to decompose the South American 30-90-day Low-Frequency Intraseasonal (LFI) and 10-30-day High-Frequency Intraseasonal (HFI) variability systematically into rotational (ROT) and inertio-gravity (IGW) components in the reanalysis data. The seasonal cycle of the LFI and HFI convective and dynamical structure is well-described by the first leading pattern (EOF1). The LFI EOF1 spatial structure during the rainy season is the dipole-like between the South Atlantic Convergence Zone (SACZ) and southeastern South America (SESA), influenced by the large-scale Madden-Julian Oscillation (MJO). During the dry season, alternating periods of enhanced and suppressed convection over South America is primarily controlled by extratropical wave disturbances. The HFI spatial pattern also resembles the SESA–SACZ structure, in response to the Rossby wave trains. Results based on normal-mode decomposition of reanalysis data and the LFI and HFI indices show that the tropospheric circulation and SESA–SACZ convective structure observed over South America are dominated by ROT modes (Rossby). A considerable portion of the LFI variability is also associated with the inertio-gravity (IGW) modes (Kelvin mode), prevailing mainly during the wet season. The proposed decomposition methodology provides new insights into the dynamics of the South American intraseasonal variability, giving a powerful tool for diagnosing circulation model issues in order to improve the prediction of precipitation.

Plain Language Summary

In this study, we proposed a decomposition methodology of the dynamic of the South American intraseasonal variability, giving a powerful tool for diagnosing circulation model issues in order to improve the prediction of precipitation. Results based on normal-mode decomposition of reanalysis data and the low-frequency intraseasonal (30-90-day) and high-frequency intraseasonal (10-30-day) variability indices show that the tropospheric circulation and SESA–SACZ convective structure observed over South America are dominated by rotational modes (Rossby and mixed waves).

1 Introduction

A substantial fraction of the submonthly to intraseasonal-scale convective variability over South America is associated with the large-scale extratropical atmospheric disturbances (Satyamurty et al., 1998; Liebmann et al., 1999; Paegle et al., 2000; Jones & Carvalho, 2002; Liebmann et al., 2011; C. S. Vera et al., 2018; Gelbrecht et al., 2018); among others. In fact, one of the most distinctive features which characterize the South America rainy season (October-April) is the presence of the South Atlantic Convergence Zone (SACZ). The SACZ varies on many time-scales and its activity is largely modulated by transient disturbances (Nogués-Paegle & Mo, 1997; Liebmann et al., 1999; Cunningham & Cavalcanti, 2006). Rossby wave trains, which can be forced by the tropical convective activity such as the Madden-Julian oscillation (MJO), induce intraseasonal variability over South America (Gonzalez & Vera, 2014; C. S. Vera et al., 2018; Adames & Wallace, 2014). This interaction between tropics and extratropics is frequently linked to the development of Pacific-South America (PSA) teleconnection pattern (e.g., (Mo & Higgins, 1998)). The existence of these disturbances was initially identified by (Liebmann et al., 1999) using 2-30-day filtered OLR anomalies. They found two preferred paths of Rossby wave train patterns in the Southern Hemisphere: one affecting the SACZ and another influencing the southwestern Amazon. In fact, the southern Amazon pattern resembles the "cold surges" phenomenon discussed in detail by (Garreaud & Wallace, 1998), (Garreaud, 2000), (Lupo et al., 2001), (Espinoza et al., 2013), among others. In addi-

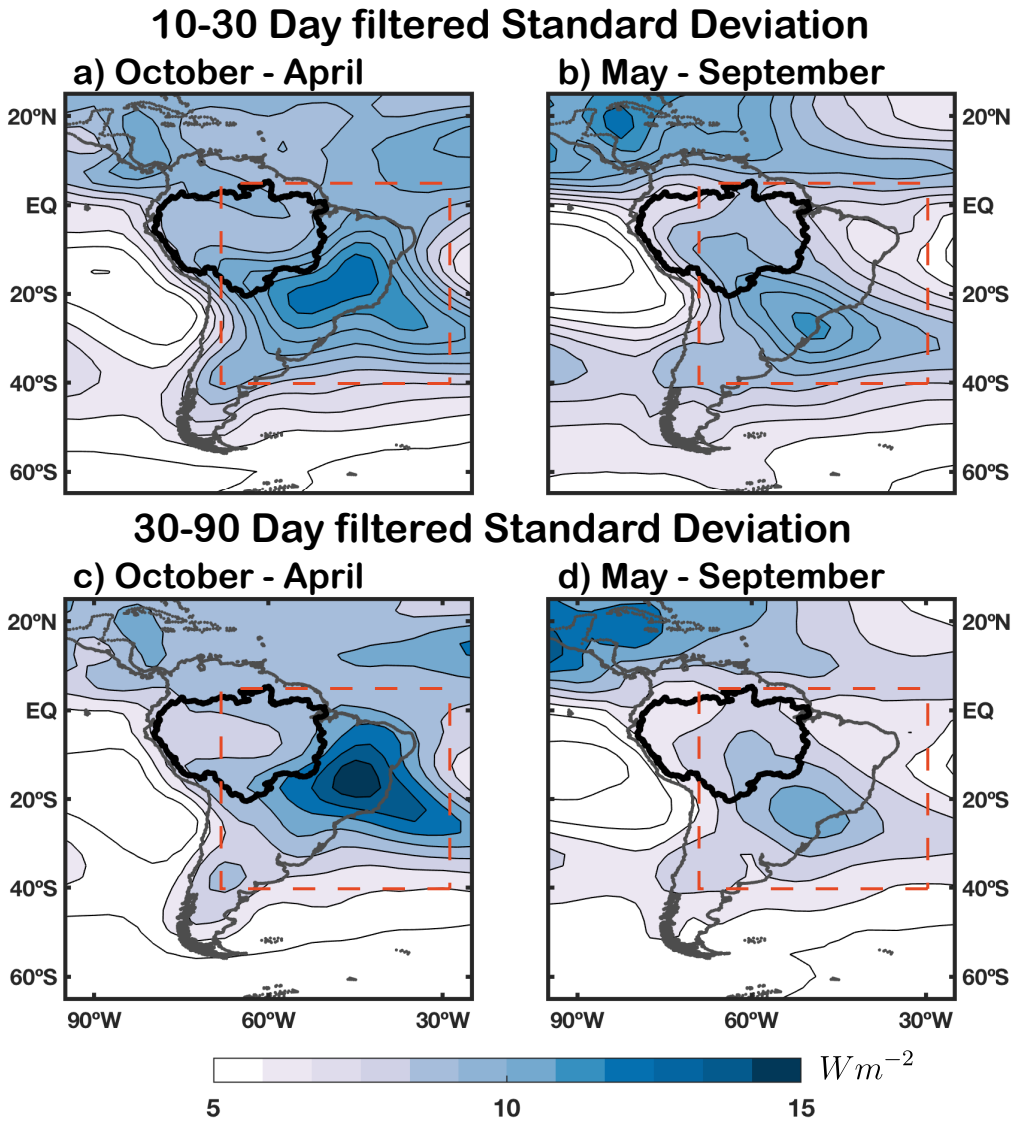

Figure 1. (Top) Standard deviation of daily 10-30-day-filtered OLR in Wm^{-2} for the (a) October-April, and (b) May-September period. (Bottom) As in the top row, but showing standard deviation of daily 30-90-day-filtered OLR. Shading interval are shown by the legend.

tion, these Rossby waveguides represent one of the preferred propagation routes in South America (Grimm & Silva Dias, 1995; Ambrizzi & Hoskins, 1997).

Recently, a new approach to study the intraseasonal variability over South America was introduced based on separating the classical intraseasonal variability into 10-30-day high-frequency intraseasonal variability and the 30-90-day low-frequency intraseasonal variability (Gonzalez & Vera, 2014; C. S. Vera et al., 2018). Early studies such as (Liebmann et al., 1999) have already documented spectral peaks at 50 days period over the SACZ and the Amazon (corresponding to the canonical MJO effect), and other peaks near 27, 16, 10, and 8 days. Similar spectral peaks were detected on observed rainfall data over the Amazon (Mayta et al., 2020). As documented by the previous references, regions located on the equatorial domain (e.g, Northeast of Brazil) also show clear spec-

tral peaks centered on about 48 days. It is widely documented that the most distinctive pattern of the 30-90-days intraseasonal variability over South America, during austral summer (corresponding to the rainy season), is the dipole-like configuration between southeastern South America (SESA) and the SACZ (Casarin & Kousky, 1986; Nogués-Paegle & Mo, 1997; Souza & Ambrizzi, 2006; C. Vera et al., 2006; C. S. Vera et al., 2018; Gelbrecht et al., 2018). In addition, recent studies demonstrated that the MJO activity is noticeable year-round over South America (Alvarez et al., 2016; C. S. Vera et al., 2018), which includes the Amazon region (Mayta et al., 2019). During the dry season (June to August), the convective features are slightly different from the rainy season. Both enhanced and suppressed convection cover a broad South America region (see Fig. 5 in (C. S. Vera et al., 2018)). On the other hand, on the 10-30-day HFI variability over South America, the dipole-like structure (SESA-SACZ) is still visible, with a stronger signal over the SESA region during the dry season (Gonzalez & Vera, 2014; C. S. Vera et al., 2018).

The low-frequency intraseasonal rainfall variability over South America, on the other hand, is not strictly associated with the forcing produced by the equatorially propagating MJO events. There are other mechanisms (e.g., through Southern Hemisphere Rossby wave trains) playing an important role in the modulation of high-frequency convective activity (Grimm & Silva Dias, 1995; Ambrizzi & Hoskins, 1997; Liebmann et al., 1999; Gonzalez & Vera, 2014; C. S. Vera et al., 2018). Indeed, recently (Mayta et al., 2019) found that on average 35% of the intraseasonal rainfall events over the Amazon (which extends from 5° to 20°) do not have the MJO as a precursor. In addition, (C. S. Vera et al., 2018) documented similar spatial patterns over South America (SESA-SACZ dipole-like), in both low- and high-frequency intraseasonal variability. These results raised some questions, for instance: which mechanisms are responsible for this configuration in the intraseasonal time-scales? (C. F. M. Raupp & Silva Dias, 2009; C. Raupp & Silva Dias, 2010) and (Ramirez et al., 2017) discussed the possibility of a nonlinear process leading to internal variability on the intraseasonal band through the nonlinear resonance of equatorial waves, associated with convective forcing, linking the diurnal variability to the modulation of the intraseasonal variability.

On the other hand, low-frequency intraseasonal precipitation over different South American regions is frequently analyzed using different MJO indices. However, most of these indices do not properly represent northward and eastward MJO propagation over tropical regions, mainly during the austral winter (Kikuchi et al., 2012; Wang et al., 2018), even over South America poorly represent its modulation in precipitation (Mayta et al., 2020). In addition, the South America intraseasonal variability is always described based on directly observed data (e.g., outgoing long-wave radiation, precipitation) and using the traditional principal component analysis. However, complex interaction in intraseasonal time-scales and shorter, indeed, need a more complex approach. In this line, (Gelbrecht et al., 2018) using more "sophisticated" techniques for the extraction of phases, demonstrated that the SESA–SACZ dipole-like precipitation structure is caused by the extratropical Rossby waves. However, some limiting factors of their approach include the irregular/intermittent character of the phenomena often misrepresented by linear techniques such as EOF, as well as the lack of detailed attribution of types and wave-numbers of the modes associated with the SESA–SACZ variability. The first drawback can be overcome by using more intrinsically nonlinear approaches like the self-organizing maps (SOM, chu2017) than a traditional linear technique such as EOFs. The second problem can be addressed by using the so-called normal mode functions (NMF), which are orthogonal eigenfunctions of the linearized primitive equations on a sphere (Kasahara & Puri, 1981; Tanaka, 1985). Indeed, recent works used NMF to characterize physical properties representative of the MJO (Žagar & Franzke, 2015; Kitsios et al., 2019), and other tropical atmospheric disturbances (Castanheira & Marques, 2015; Raphaldini et al., 2020). An earlier study (Baer, 1972) suggested a two-dimensional index ($index = s+n$) as a measure of horizontal scale as in (Kasahara, 1980) (see his Fig. 5). Where s and n are the zonal wavenumbers and meridional indices, respectively. Thus, in this study we will

project 3D atmospheric fields onto normal modes of the global primitive equations, based on the (Kasahara & Puri, 1981) approach, to determine the modes that more closely describe the observations.

Therefore, the main goal of this study is to further explore the high- and low-frequency intraseasonal variability over South America. Firstly, through the leading EOFs, explore how the low-frequency intraseasonal is influenced by the high-frequency intraseasonal. To assess the physical mechanism associated with the 30-90-day Low-frequency (hereafter LFI), and the 10-30-day High-frequency (hereafter HFI) we computed a decomposition of both frequencies in terms of normal-mode functions by performing linear regressions between the indices and normal-mode amplitudes. The normal-mode functions constitute a complete basis for the atmospheric circulation (i.e., atmospheric wind and pressure). Therefore, this procedure will provide the most relevant modes contributing to the presence of dipole configuration on 30-90-day LFI, as well as the modes associated with the extratropical Rossby wave trains.

Several key research issues relevant to intraseasonal oscillation over South America, which were not explored in previous studies, will be addressed in the present study.

The paper is organized as follows. Section 2 presents a brief description of the data and methodologies. In section 33.1, we described the seasonal cycle of LFI and HFI variability, including their dynamical mechanisms in section 33.2. The relationship between the LFI and HFI is discussed in section 33.3. Section 33.4 analyzes the normal-mode components related to the LFI and HFI variability over South America. Finally, the main results are summarized and discussed in section 4.

2 Data and Methodology

2.1 Data

Satellite-observed outgoing longwave radiation (OLR) data are used as a proxy for the large-scale convection over South America. The OLR data was obtained from the National Oceanic and Atmospheric Administration - NOAA (Liebmann & Smith, 1996). Figure 1 shows the geographical standard deviation distribution of the LFI and HFI filtered OLR over 1980-2016 and considering the South American monsoon period (October-April, hereafter rainy season) and the absence of SAMS (May-September, hereafter dry season) period. Over South America, during the Oct-Apr period, both LFI and HFI show peak activity over the mean position of the SACZ (Figures 1a, c). This signal extends toward the South Atlantic Ocean and southeastern Amazon. Similar variance was documented by (Liebmann et al., 1999) during austral summer (see their Fig. 3a). On the other hand, the LFI and HFI convective activity during the austral dry period (May-Sep) peaks over southeastern South America. Areas with maximum standard deviation values in HFI extends towards the north, covering almost the entire Amazon (Fig. 1b).

The dynamical fields used to analyze the South America intraseasonal variability comes from the European Centre for Medium-Range Weather Forecast reanalysis (ERA-Interim, (Dee et al., 2011)). The ERA-Interim dataset is a 2.5° horizontal resolution grid, with daily observations for the 1980-2016 period.

2.2 Methodology

2.2.1 Filtering and empirical orthogonal function (EOF) Technique

Daily anomalies of the convection and dynamical fields are calculated at each grid point by subtracting the first three harmonics (i.e., the annual cycle and first 2 harmonics) of the entire 36-years time-series in order to remove the seasonal cycle. The LFI and HFI filtered anomalies are obtained by applying Fast Fourier Transform (FFT), consid-

ering a frequency domain of 30-90-days and 10-30 days, respectively. Filtered OLR within the South America domain (red box in Fig. 1) is then submitted to a covariance matrix EOF analysis that retains the local variance of the EOF fluctuations. As in (Kiladis et al., 2014), EOFs are computed considering the entire record (from 1979-2015) but centered on each day of the calendar year using a sliding window. A 121-days (61-days) window lengths, for the LFI (HFI), are considered for the analysis. This approach, indeed, takes into account for the complex convective propagation over the region, and better characterize the seasonal variation of the intraseasonal variability. The first principal component (PC1) time series of the EOF is used to compute regression analysis and to define LFI and HFI events. In addition, the leading EOF time series is used in the decomposition of the LFI and HFI in terms of the normal-mode functions.

2.2.2 Global Normal-Mode Function (NMF) Expansion

Given that the reanalysis data are provided for the entire globe, it is desirable to associate them with normal modes of the atmospheric equations on the sphere. (Kasahara & Puri, 1981) introduced a methodology to project 3D Global reanalysis data by projecting it onto a basis of normal mode functions, solutions of the linearized atmospheric primitive equations on the sphere. The linearized system of the atmospheric primitive equation in sigma coordinates and the vertical direction is given by:

$$\frac{\partial u}{\partial t} - 2\Omega v \sin(\phi) = -\frac{g}{a\cos(\phi)}\frac{\partial h}{\partial \lambda}, \tag{1}$$

$$\frac{\partial v}{\partial t} + 2\Omega u \sin(\phi) = -\frac{g}{a}\frac{\partial h}{\partial \phi}, \tag{2}$$

$$\frac{\partial}{\partial t}\Big[\frac{\partial}{\partial \sigma}\Big(\frac{g\sigma}{R\Gamma_0}\frac{\partial h}{\partial \sigma}\Big)\Big] - \nabla \cdot \mathbf{V} = 0, \tag{3}$$

where $\mathbf{V} = (u, v)$ is the velocity field given by its zonal and meridional components, Ω is the Earth's rotation rate and a its radius. $h = P/g$ represents the modified geopotential height, with P the pressure field and g the acceleration of gravity. $\Gamma_0 = \kappa T_0/\sigma - dT_0/d\sigma$ is the static stability parameter, where $T_0 = T_0(\sigma)$ is the globally horizontally averaged temperature. The boundary conditions are no-penetration conditions at the top and at the bottom ($\sigma = 0$ and $\sigma = 1$). The solutions of this coupled system are obtained by performing a separation of variables into a horizontal and a vertical structure:

$$\begin{bmatrix} u'(\lambda,\phi,\sigma,t) \\ v'(\lambda,\phi,\sigma,t) \\ h'(\lambda,\phi,\sigma,t) \end{bmatrix} = G(\sigma) \begin{bmatrix} u(\lambda,\phi,t) \\ v(\lambda,\phi,t) \\ h(\lambda,\phi,t) \end{bmatrix}, \tag{4}$$

where the vertical structure function is given by $G(\sigma)$ and is expanded in terms of a basis of orthonormal basis functions:

$$G(\sigma) = \sum_{m=1}^{M} G_m(\sigma). \tag{5}$$

The horizontal structure function is given by the product of an oscillatory term in time and a spatial structure as follow:

$$\mathbf{U}(\lambda,\phi,t) = \sum_{n=0}^{N}\sum_{k=0}^{K} \mathbf{H}_n^k(\lambda,\phi) e^{(-i\omega_n^k t)}, \tag{6}$$

where n and k are the meridional and the zonal mode indices, respectively. The spatial structure $\mathbf{H}_n^k$ is described by Hough modes. Given a vector field $\mathbf{X}$, given on a

discrete grid over the sphere, the projection of $\mathbf{X}$ onto the basis of normal mode function is obtained by using the inner product from the vertical eigenvalue problem:

$$\mathbf{X}(\lambda, \phi, \sigma_j) = \sum_{m=1}^{M} \mathbf{X}_m(\lambda, \phi) G_m(\sigma_j), \tag{7}$$

providing a set of horizontal structures $\mathbf{X}_m$, for each vertical level $j = 1, ..., J$, and $G_m(\sigma_j)$ is a discretized version of the vertical structure function $G_m(\sigma)$ via finite differences. $\mathbf{X}_m$ is then projected onto the basis of Hough functions to obtain the normal mode coefficient associated with indices (m, n, k):

$$\chi_{mnk} = \int_0^{2\pi} \int_{-\pi/2}^{\pi/2} \mathbf{X}_m \cdot \left[\mathbf{H}_n^k\right]^* \sin(\phi) d\phi d\lambda. \tag{8}$$

Based on this, the vector field $\mathbf{X}$ is expressed as a sum of components corresponding to each of the elements of the basis of the normal mode functions with their respective amplitudes:

$$\mathbf{X}(\lambda, \phi, \sigma_j) = \sum_{m=1}^{M} \sum_{n=0}^{N} \sum_{k=0}^{K} \chi_{kmn} G_m(\sigma_j) \mathbf{H}_n^k(\lambda, \phi). \tag{9}$$

In this study, we use the open-source software MODES (Žagar et al., 2015) that performs these operations given the horizontal winds and geopotential height data from the reanalysis.

2.2.3 Computation of the Low- and High-frequency Intraseasonal in Modal Space

In this work, we used indices which describe the tropical and extratropical precursors associated with the high and low frequency intraseasonal variability. The resulting precipitation pattern in South America will be assessed in terms of NMF expansion following (Žagar & Franzke, 2015). These authors, for instance, introduced a methodology to decompose the widely used all seasons multivariate MJO index (M. C. Wheeler & Hendon, 2004) into normal mode functions. They performed a linear regression of the RMM indexes $Y_i(t)$, $i = 1, 2$ against the normal mode function coefficients:

$$\mathcal{R}_{kmn}^i = \frac{1}{N-1} \sum_{t=1}^{N} \frac{(\chi_{kmn}(t) - \overline{\chi}_{kmn})(Y_i(t) - \overline{Y}_i)}{\mathrm{Var}(Y_i(t))} \tag{10}$$

where $\mathcal{R}_{kmn}^i$ is the regression coefficient of i-th index against the normal mode with mode indices (k, m, n). In addition, the complex coefficient of $\mathcal{R}_{kmn}^i$ describes the projection of the southern hemisphere circulation associated with the LFI and HFI index. The relative importance of each normal mode to the given i-th index is obtained by its variance as follow:

$$V_{kmn}^i = g D_m \mathcal{R}_{kmn}^i \left(\mathcal{R}_{kmn}^i\right)^* \tag{11}$$

where g is the acceleration of gravity, D_m is the equivalent depth of the m-th vertical mode, and * indicates the complex conjugate, respectively (more details in (Žagar & Franzke, 2015)).

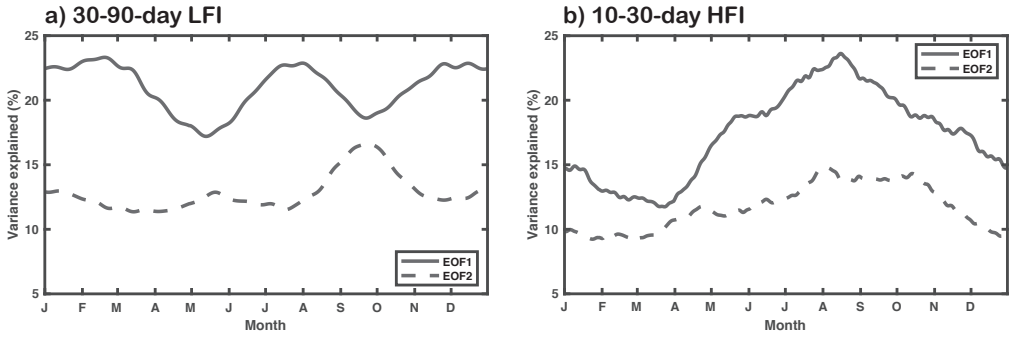

Figure 2. Daily eigenvalues corresponding to an EOF analysis of (a) 30-90-day Low-frequency Intraseasonal, and (b) 10-30 High-frequency Intraseasonal filtered OLR. EOFs are calculated between 40°S-5°N and 70°W-30°W (red box in Fig. 1) using a 121-day and 61-day sliding window, respectively.

3 Results

3.1 EOF results: Seasonal Cycle of the LFI and HFI variability

The spatial pattern associated with both the LFI and HFI variability follows the maximum activity observed in Figure 1 and documented previously (e.g., (C. S. Vera et al., 2018; Gelbrecht et al., 2018; Mayta et al., 2019)).

Figure 2a shows the seasonal cycle of EOF1 and EOF2 for each day obtained from the EOF analysis applied to the 30-90-day Low-frequency filtered OLR. The first two modes explain on average about 22% and 12% of the total variance, respectively. These modes are distinct and well-separated from the rest, following the (North et al., 1982) criterion (not shown). The variance explained by the EOF1 peaks during mid-February, August, and mid-February.

On the other hand, Fig. 2b shows the seasonal cycle of EOF1 and EOF2 corresponding to the 10-30-day High-frequency filtered OLR. The HFI EOF1 and EOF2 explain on average about 19% and 10% of the total variance, respectively. The variance explained by the HFI EOF1 peaks, as documented by (C. S. Vera et al., 2018)(see their Fig. 4f), during mid-August. Its maximum activity during austral winter yields some clues about how HFI variability in winter plays an important role. This hypothesis will be explored in section 33.3.

3.2 South America Intraseasonal Variability: Dynamical Mechanisms

LFI and HFI circulation and convection structure presented in this section are based on linear regression. We regress each index against dynamical and convective fields (OLR, velocity potential, streamfunction, and winds at 200-hPa) on the global domain. The linear regression results based on this index are then scaled to -30 W m^{-2} anomaly in OLR on day 0. When each index reaches its maximum negative value is defined as day 0. The statistical significance of these results is assessed based on the two-tailed Student's t-test. This method takes into account the correlation coefficients and an effective number of independent samples (degrees of freedom) based on the decorrelation timescale, as in (Livezey & Chen, 1983) (more details in (Kiladis & Weickmann, 1992; Straub & Kiladis, 2002)). Two sub-seasons are considered for the analysis: October-April characterized mainly by the presence of the active SAMS period and May-September as the absence of this forcing.

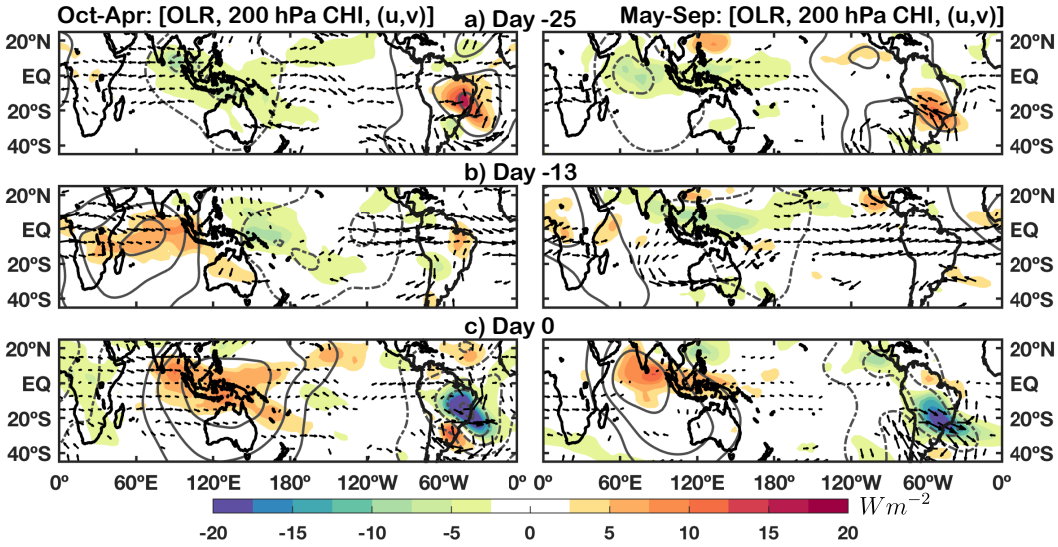

Figure 3. Regressed values of OLR (shading), velocity potential (contours), and winds (vectors) at 200-hPa, based on -30 W m^{-2} anomaly in LFI OLR index on day 0. Shaded OLR in W m^{-2} are shown by the legend. The velocity potential contour interval is 7.5x10^5 m^2s^{-1}. Positive (negative) contours are solid (dashed). The longest wind vectors correspond to 10 m s^{-1}, and are plotted only where either the u or v component is significant at the 95% level or greater.

3.2.1 South America 30-90-day Low-Frequency Intraseasonal variability (LFI)

Figure 3 depicts the evolution of tropical convection and implied large-scale circulation (upper-level velocity potential and winds) during a typical oscillation for the October-April (left column) and May-September season (right column). The large convection anomalies along the equator in the Maritime continent (Fig. 3a) propagate eastward to South America resulting in the SESA-SACZ dipole-like configuration (Fig. 3c). Despite the EOF calculations are made into the South America domain, as in other EOF-based analyses of the MJO, the upper-level structure exhibits a zonal wavenumber-1 structure in the equatorial belt. For instance, at day 0 (Fig. 3c) shows a strong positive center over the Maritime Continent and the negative center of action over South America.

On the other hand, Figure 3 (right column) shows the large-scale convection pattern and upper-level divergence for the May-September period. Some differences in eastward propagation phase speed for the circulation and OLR anomalies is evident in the regression maps. The OLR anomalies, initially over the Maritime Continent (day -25 in Fig. 3a), propagate eastward creating a condition for convection in a broad southern South America (day -25 in Fig. 3c). The convective evolution, from day -25, shows a clear resembles the spatial structure widely-documented by using diverse MJO indices (e.g., (M. C. Wheeler & Hendon, 2004; Kiladis et al., 2014)). The upper-level divergence (negative velocity potential) shows a positive center over the Indian Ocean and a more diffuse negative center of action over South America. The convective-dynamical evolution observed during October-April, even during the May-September months, clearly resembles the composite maps made using the OMI indices in (Mayta et al., 2020). Owing to the LFI index was calculated using a sliding window, our results demonstrated that this index properly represents the seasonal large-scale MJO impacts (Kikuchi et al., 2012; Wang et al., 2018).

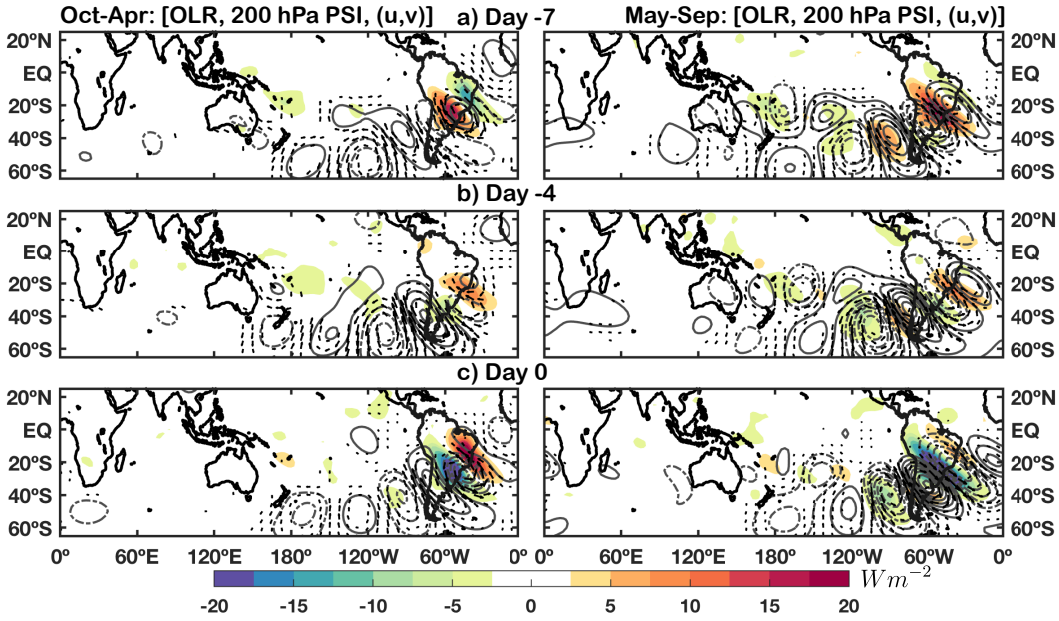

Figure 4. Regressed values of OLR (shading), streamfunction (contours), and winds (vectors) at 200-hPa based on HFI index. All fields are scaled to a -30 W m^{-2}. Shaded OLR in W m^{-2} are shown by the legend. Streamfunction contour interval is 2x10^6 m^2 s^{-1}. Positive (negative) contours are solid (dashed). The longest wind vectors correspond to 10 m s^{-1}, and are plotted only where either the u or v component is significant at the 95% level or greater.

3.2.2 South America 10-30-day High-Frequency Intraseasonal variability (HFI)

Similarly to the previous section, here the HFI index is regressed against dynamical and convective fields on the global domain. Figure 4 shows the regressed values of OLR (shading), 200 hPa streamfunction (contours), and winds (vectors), based on 10-30 filtered OLR for days -7, -4, and day 0. The regression maps were separately calculated for the Oct-Apr (left column) and May-Sep (right column) season. During the Oct-Apr period, at day -7, as in (C. S. Vera et al., 2018), suppressed convection occurs over the SESA region (Fig. 4a). At the same time, a well-developed series of upper-level alternating cyclones and anticyclones extending eastward and equatorward are observed. Then, 3 days later enhanced convection signal starts over Argentina, as the time of the wave trains propagate towards the South Atlantic Ocean (Figure 4b). At day 0 (Fig. 4c), convection peaks over the SESA region and the Rossby wave trains are propagating equatorward. Our results are consistent with (Liebmann et al., 1999) who showed similar OLR and large-scale features associated with the submonthly variability over the SACZ region (see their Fig. 6).

On the other hand, during the May-Sep season, the suppressed (day -7) and enhanced (day 0) convection cover a broad area of South America with a northwest-southeast band extending to the adjacent ocean. Recently, (C. S. Vera et al., 2018) also showed similar strong convection over the SESA region extending their signal towards the southern Amazon, as observed in Fig. 4c. Similarly, the convection activity observed during the dry period is accompanied by a highly statistically significant Rossby wave trains. The wave trains, unlike the Oct-Apr period, stretches eastward and equatorward from the Western Pacific and South Pacific Convergence Zone (SPCZ) with an arch-like struc-

ture. This pattern resembles the spatial features associated with the PSA-like mode documented by (Mo & Higgins, 1998). Many of the extratropical wave trains in the upper-tropospheric (Figure 4) are, in many instances, directly forced by the divergent outflow from regions of enhanced equatorial convection, such as the MJO convection (Jin & Hoskins, 1995; Mori & Watanabe, 2008). Moreover, considering that the SPCZ has a broad multiscale variability (Matthews, 2012), including the submonthly timescale, previous studies have already suggested the interactions between convection over South America and the SPCZ trough Rossby wave trains (Grimm & Silva Dias, 1995; Gonzalez & Vera, 2014).

Overall, the dipole-like SESA–SACZ precipitation pattern is caused primarily owing to the HFI by the southern hemisphere Rossby waves. Other wave modes to characterize the HFI will be explored in detail in the next sections.

3.3 The relationship between the LFI and HFI variability

Recent studies documented that a large part of the intraseasonal SESA-SACZ dipole-like configuration over South America is due to extratropical wave disturbances such as Rossby wave trains (Gelbrecht et al., 2018). (Mayta et al., 2019), for instance, found that the equatorial MJO precursors are responsible for about 65% of the total LFI events detected over the Amazon. Considering that the Amazon region extends from 5°N to 20°S (tropical domain), the authors also suggested "other" mechanisms responsible for the remaining LFI events, such as Rossby wave trains in the Southern Hemisphere. Therefore, using similar criteria proposed by (Mayta et al., 2019), LFI events over South America are defined considering their PC1 time series. According to this criterion, the 30-90-day PC1 time series, during the event, must be lower than -1.0 standard deviation. The minimum duration of the event must be 5 days (like a single MJO index phase average duration). To verify that a singular LFI event is preceded by a large-scale MJO active phase propagating into the South America region, two widely-used existing MJO indices are considered: (1) OLR-based MJO (OMI index; (Kiladis et al., 2014)); and (2) combined convectively- and dynamically-based MJO (RMM index; (M. C. Wheeler & Hendon, 2004)). Finally, the occurrence of each LFI event is attributed to the associated precursor. We divided all precursors into three main types: (1) tropical precursors (T) when a LFI event is preceded by the MJO eastward-propagation; (2) extratropical precursor (E) associated with the extratropical Rossby wave trains; and (3) other precursors (OP) means that LFI events do not have precursors of either type 1 or 2 above.

Table 1 summarizes the total LFI events recorded for the 1980-2016 period. In total 147 events were recorded for the entire period, which means around ∼4 per-year. As expected from previous sections, LFI events are mainly associated with the large-scale MJO eastward propagation, responsible for the spatial structure observed in Fig. 3. On average 70% of the total events are associated with the MJO activity, as also detected by the MJO indices. However, about 20% of these events are mainly preceded by HFI activity. Another important point to stands out is the existence of a significant percent ($\sim 20\%$) of occurrences of LFI events preceded by tropical and extratropical precursors acting simultaneously. Even though the HFI events show an almost constant activity through the year (not shown), these events play an important role in organizing convection mainly during the dry season. The remaining events, as appears in Table 1, are explained by other precursors. Other precursors could be associated, for instance, with disturbances which act at the same frequency, such as the westward propagating Rossby equatorial waves (M. Wheeler & Kiladis, 1999; M. C. Wheeler et al., 2000). Indeed, even events with tropical precursors in many instances could be associated with the convectively-coupled Kelvin waves (Liebmann et al., 2009). Finally, we observed a deficit of LFI events during the El Niño years (e.g., 1986/87, 1997/98, 2009/10) and the exceptional warm SST conditions in the tropical Atlantic, occurred in 2005 and 2010 (Table 1).

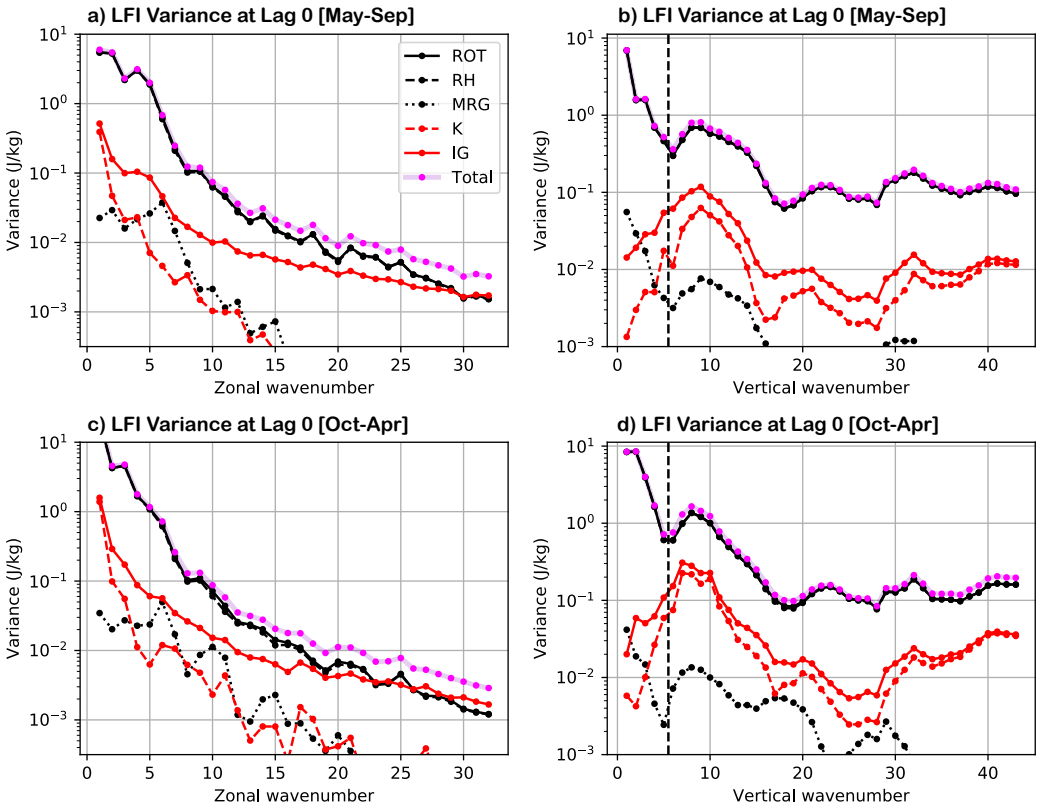

Figure 5. The LFI index variance explained by zonal (left column) and vertical (right column) mode. The variance at the top (bottom) corresponds to the May–September (October–April) period. Dashed lines mean the specific mode contribution to each two-main types: Rotational (ROT, black) or Intertio-Gravity (IGW, red).

In the next section, we will use a normal mode decomposition of the LFI and HFI to describe the modal structure as well as the horizontal and vertical scales of the perturbations associated with both indices.

3.4 Normal-modes Components of the South America intraseasonal variability

The interaction between tropical convection and large-scale systems is characterized by energy conversion processes (Silva Dias et al., 1983). In this sense, the analysis of normal-modes decomposition of the intraseasonal variability constitutes a methodology for diagnosing the energy responsible for the circulation. In this approach, the solution of the vertical structure associated with intraseasonal variability makes it possible to analyze the energetics for each of the vertical modes, separately, in external and internal modes (Figures 5,7). While in the energy distribution between the horizontal modes (Figures 6,8, and A1), the eigenvalues (normal modes) are classified in modes gravitational (Kelvin and gravity waves; IGW) and rotational (Rossby and mixed waves; ROT).

3.4.1 Normal-modes Components: 30-90-days LFI

Figure 5 displays the contribution of each mode (zonal and vertical) to the total variance. On large-scales (k=1–5) most of the LFI index variance is well-described by

Rossby modes, with non-negligible contributions of Kelvin and Mixed Rossby-gravity modes accounting for about 10% of the variance. Our results are in agreement with (Žagar & Franzke, 2015), where the authors documented the same planetary modes for the MJO. For more internal modes (lower equivalent depth), the contribution of inertio-gravity waves become more comparable and in the same order of Rossby modes. It is also observed similar LFI-associated modes for both the May to Sep and Oct-Apr periods.

Figures 5b,d reveal the leading vertical modes with a strong contribution of barotropic modes on the troposphere, while barotropic Kelvin and inertio-gravity modes are less prevalent since these modes are associated with large-scale convection. Baroclinic Rossby modes, although still prevalent, they account for less variance than the barotropic ones, while the contribution of baroclinic Kelvin waves becomes more important (especially for m=7–11). The distribution of variance is similar throughout both wet and dry seasons. The most noticeable difference is the larger contribution of Kelvin waves during the wet season, which was also expected (Figure 5c).

Figure 6 shows the regression horizontal structure associated with the LFI index for a pressure level close to ∼200–hPa. The projected circulation represents the contribution of the rotational modes (ROT, Fig. 6a,d), inertio-gravity modes (IGW, Fig. 6b,e), and the total fields (Fig. 6c,f). The calculations are computed separately for the October-April and May-September season, respectively, and at lag 0 only (as in Fig. 3c). Figures 6c,f suggest that majority of LFI circulation, such as the mid-latitude wave-trains, is dominated by ROT modes. However, for the MJO large-scale, the ROT mode (k=1 Rossby wave) is the dominant mode associated with the MJO (Žagar & Franzke, 2015). These wide-documented mid-latitude wave-trains (e.g., (C. S. Vera et al., 2018; Gelbrecht et al., 2018), and references therein) present different aspects comparing the dry and wet seasons that can be explained in terms of the spectrum of their ROT variance in each season (Figure 5). Indeed, these wave-trains acquire a more clear pattern in the dry season, since in this season there is less energy in global scale wave-numbers k=0–3 and more energy in wave-numbers k=4–6 when compared to the wet season. This result was also expected since the dominant LFI pattern from May-September is mainly influenced by the extratropical disturbances rather than large-scale MJO eastward-propagation (Figure 3 and Table 1). Figure 3b also depicts westerly winds along the equator in the ahead of the region of strong convection (South America) resembling the structure of the k = 1 eastward propagating IGW mode (i.e., the Kelvin wave). Indeed, as observed in Figure 5c for the wet season, the contribution of Kelvin waves within IGW decay rapidly, and therefore within or compared to the total fields as well. A relative IGW max signal over the Andes observed in Fig. 5e, is a result of the interaction of the Southern Hemisphere winter upper-level westerlies that are stronger at this latitude. To better-represent the MJO upper-level zonal wavenumber-1 (k=1) structure in the equatorial belt, we plotted in Figure A1 velocity potential instead of streamfunction. The upper-level wind anomalies are mainly zonal (Fig. A1b) with a wavenumber-1 structure comparable to those in previous studies of (Hendon & Liebmann, 1994; Kiladis et al., 2005; Adames & Wallace, 2014). The pattern is suggestive of an equatorial Kelvin wave signature that extends from South America, being barely equatorially trapped with a band of westerlies between 10°N/S. On the other hand, upper-level divergence over South America, even in IG modes, highlights the presence of wave trains (Fig. A1e).

3.4.2 Normal-modes Components: 10-30-days HFI)

Following equation 11, Figure 7 shows the contribution of the various modes to the HFI index. The results show that the distribution of the variance of the regression coefficients is dominated by rotational modes. For instance, the variance distribution on the zonal mode index k shows that HFI is strongly dominated by Rossby modes for large scale modes (k=1–7). However, the contribution of the Rossby mode presents a fast decay as k increases in a way that for smaller-scale modes (i.e., $k \geq 15$) when the con-

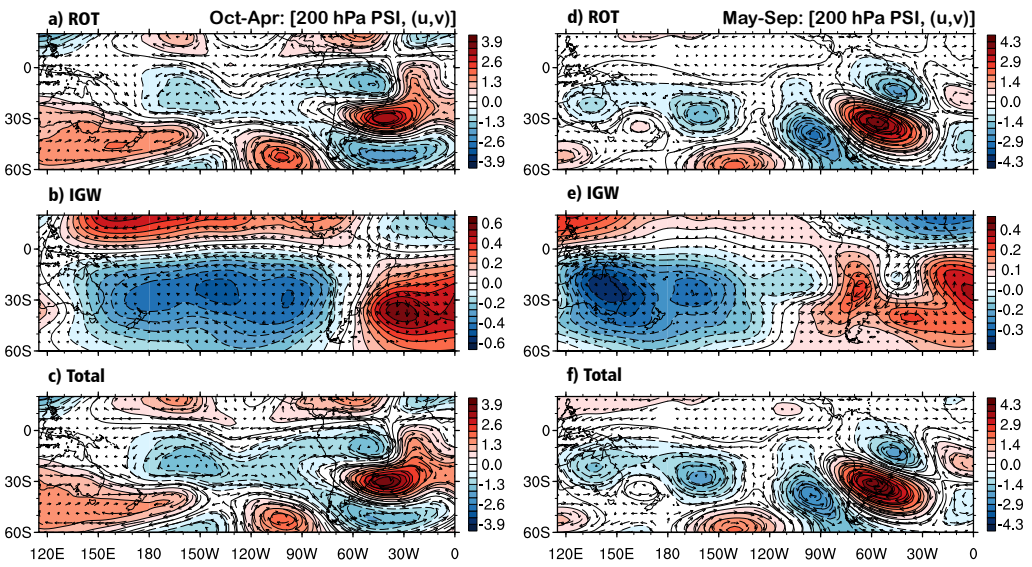

Figure 6. Low-frequency intraseasonal (LFI) regression patterns of upper-level (200–hPa) winds (vectors) and streamfunction (filled contours). (a), (d) are rotational components; (b), (d) are inertio-gravity components; and (c), (f) are the total fields. Regressions patterns in the left (right) column corresponds to the October–April (May–September) period. Streamfunction contour interval is 1x10^6 m^2 s^{-1}. Positive (negative) values are shown in red (blue). The longest wind vectors correspond to 10 m s^{-1}.

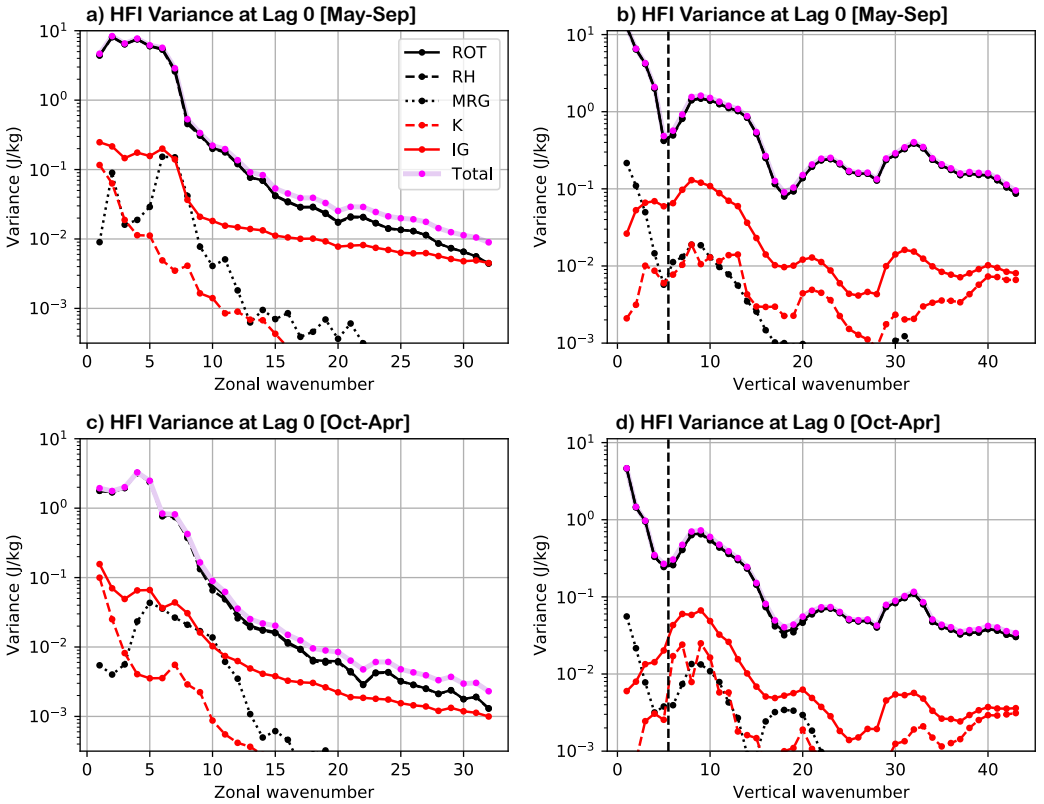

Figure 7. As in Figure 5, but for the HFI index.

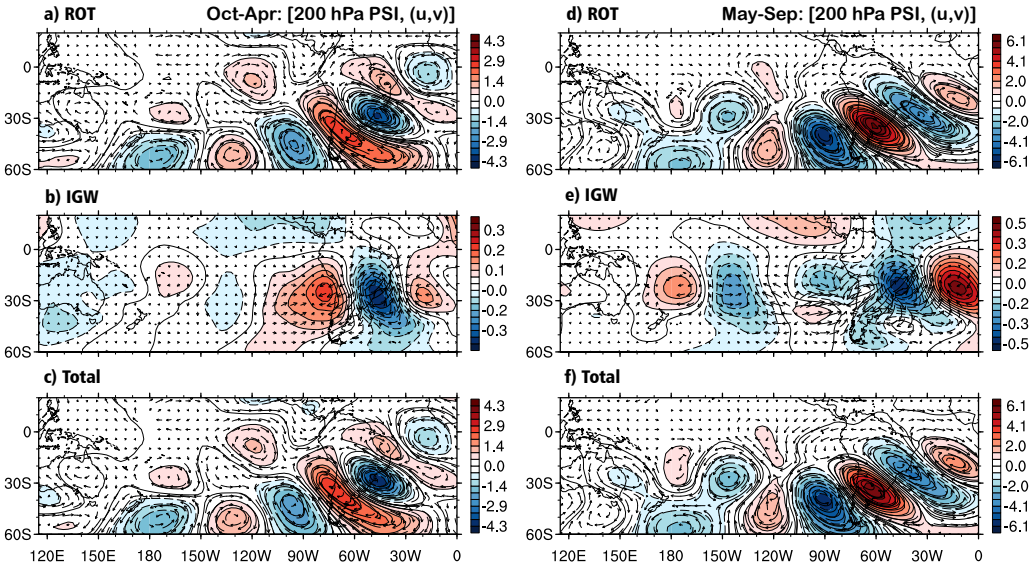

Figure 8. As in Figure 6, but for the HFI index.

tribution of inertio-gravity waves become more relevant. On the other hand, as expected, the contribution of equatorially confined modes such as Kelvin and mixed Rossby-gravity modes are less relevant compared to their contribution to LFI (Figures 7a, c). The vertical distribution of the variance shows that HFI variability is more associated with modes with barotropic structure in the troposphere (m=1–5; Fig. 7b, d). Considering that HFI represents here higher latitudes dynamics, lower-order modes, with the barotropic mode becoming dominant, were expected (Kasahara & Puri, 1981; Silva Dias & Bonatti, 1985). In addition, a strong contribution of modes with baroclinic structure is observed in modes with large m (m=6–15), with peaks at m=8–9). Peaks at m=8–9 are quite evident for both seasons, stronger during the May-Sept period, as also documented in (Silva Dias & Bonatti, 1985). Differences in the distribution of variance with the mode index is very similar in both dry and wet seasons. The most significant difference noticed is the larger contribution of Mixed Rossby-Gravity (MRG) modes during the dry season (Figures 7b, d). Indeed, it could be explained by the fact that this mode has asymmetric wind structure concerning the equator and can have different responses owing to solar forcing depending on the time of the year (Silva Dias et al., 1983).

The decomposition of the regressed circulation fields (upper-level streamfunction and winds) onto IGW and ROT components associated with HFI is presented in Figure 8. According to Figures 8c, f the average HFI circulation is rotational, which also expected from Figure 7. In other words, we can reconstruct the basic features of the previously observed structures in Figure 4 using just rotational modes. The same predominance, by rotational modes, is found for both seasons. Comparing with the pattern of the regressed LFI fields, on the other hand, it is noticeable that IGW modes have a more important contribution of wave-numbers k=4–7, rather than the rapidly decaying variance of the IGW modes associated with LFI.

4 Summary and Conclusions

In this study, we presented an alternative approach to analyzing South America intraseasonal variability, based on normal mode decomposition. This methodology involves decomposition of circulation and pressure fields into normal-mode functions (NMF),

which was applied in previous studies to the MJO (Žagar et al., 2015; Franzke et al., 2019). In particular, we focus on the interaction between mid-latitude wave disturbances and the classical equatorial MJO impact in the intraseasonal signal over South America.

We started by separating intraseasonal South America variability into 30–90-day Low-Frequency Intraseasonal (LFI); and 10–30-day High-Frequency Intraseasonal (HFI) as in (C. S. Vera et al., 2018). For LFI and HFI, the leading patterns were studied through EOF analysis as in (Kiladis et al., 2014). EOFs were computed onto the region of maximum intraseasonal signal indicated by the red box in Figure 1. The period considered for the analysis was from 1980 to 2016, but centered on each day of the calendar year, using a sliding window to take into account the seasonal migration of the intraseasonal signal (Kiladis et al., 2014; Wang et al., 2018).

The results show that the PC1 (dominant mode for both LFI and HFI; Figure 2) time series well-described the intraseasonal variability in South America. Considering the LFI, the presence of dipole-like SESA-SACZ structure (Casarin & Kousky, 1986; Nogués-Paegle & Mo, 1997; C. S. Vera et al., 2018; Gelbrecht et al., 2018) is the most distinctive feature observed over South America during the rainy season (Oct–Apr). This structure, as documented in the references above, is primarily caused by the large-scale eastward-moving MJO (Figure 3). LFI events showed maximum activity during the rainy season, where events preceded by the MJO are well-described by different MJO indices (Table 1). Even though during the May–Sep season an apparent presence of the large-scale MJO (Fig. 3) is observed, the enhanced convection over the SESA region is mainly controlled by extratropical wave disturbances (Table 1). Our results, on the other hand, demonstrated that the HFI spatial pattern also resembles the so-called SESA–SACZ structure, in response to the Rossby wave trains as in (Grimm & Silva Dias, 1995; C. S. Vera et al., 2018). In addition, HFI events show an almost constant activity throughout the year, playing an important role mainly during the dry season. We found that on average about 20% of the LFI events are preceded by HFI events. Another 20% of the events enhanced convection is preceded by both precursors (Table 1).

We also presented a decomposition of the South American intraseasonal variability (LFI and HFI) into rotational (ROT) and inertio-gravity (IGW) components. Using a linear regression between the complex expansion coefficients of the NMF representation of the reanalysis data and daily values of the LFI index, our results show that rotational (Rossby mode) dynamics is the most important mode contributing to the tropospheric circulation and the SESA–SACZ convective structure observed over South America (Figures 5, 6 and, A1). However, considerable portion of the LFI variability is associated with the inertio-gravity waves (IGW) modes (e.g., Kelvin mode), prevailing mainly during the rainy season (Figures 5c, 8b, A1b). During the dry season, in contrast, the circulation and associated convective signal variability are primarily represented by ROT modes as also observed in the precursors of the intraseasonal convective signal (Figures 6d, A1d, and Table 1). In addition, zonal and vertical mode contribution to the total variance revealed a strong contribution of barotropic modes rather than other vertical modes (Figure 5a, b). Considering that the South America Monsoon System constitutes an important heat source, our results also yield clues about the preferential interaction between the intraseasonal time scale and others, for instance through tropical extra-tropical interactions of the normal modes (C. F. M. Raupp et al., 2008). HFI variability (Fig. 4), on the other hand, as was depicted for LFI, is dominated by rotational modes throughout the year (Figure 7).

Subseasonal to intraseasonal variability over South America involves a complex and nonlinear interaction between them. The normal mode approach is, indeed, an alternative way of evaluating the intraseasonal variability over South America. The proposed decomposition methodology of low- and high-frequency intraseasonal can provides insights into the dynamics of the intraseasonal variability in South America, providing a

powerful tool for diagnosing model problems when comparing normal mode decomposition of reanalysis and model predictions of precipitation.

Acknowledgments

VM was supported by the National Science Foundation under Grant AGS-1841559. Interpolated OLR and ERA-Interim Reanalysis data are provided by the NOAA/ESRL.

References

Adames, A. F., & Wallace, J. M. (2014). Three-dimensional structure and evolution of the mjo and its relation to the mean flow. *Journal of the Atmospheric Sciences*, *71*(6), 2007-2026. doi: 10.1175/JAS-D-13-0254.1

Alvarez, M. S., Vera, C. S., Kiladis, G. N., & Liebmann, B. (2016, Jan 01). Influence of the madden julian oscillation on precipitation and surface air temperature in south america. *Climate Dynamics*, *46*(1), 245–262.

Ambrizzi, T., & Hoskins, B. J. (1997). Stationary rossby-wave propagation in a baroclinic atmosphere. *Quarterly Journal of the Royal Meteorological Society*, *123*(540), 919-928. doi: 10.1002/qj.49712354007

Baer, F. (1972, 05). An Alternate Scale Representation of Atmospheric Energy Spectra. *Journal of the Atmospheric Sciences*, *29*(4), 649-664. doi: 10.1175/1520-0469(1972)029⟨0649:AASROA⟩2.0.CO;2

Casarin, D. P., & Kousky, V. E. (1986). Anomalias de precipitação no sul do brasil e variações na circulação atmosférica. *Revista Brasileira de Meteorologia*, *2*, 83-90.

Castanheira, J. M., & Marques, C. A. F. (2015). Convectively coupled equatorial-wave diagnosis using three-dimensional normal modes. *Quarterly Journal of the Royal Meteorological Society*, *141*(692), 2776-2792. doi: 10.1002/qj.2563

Cunningham, C., & Cavalcanti, I. F. A. (2006). Intraseasonal modes of variability affecting the south atlantic convergence zone. *International Journal of Climatology*, *26*(9), 1165-1180. doi: 10.1002/joc.1309

Dee, D. P., Uppala, S. M., Simmons, A. J., Berrisford, P., Poli, P., Kobayashi, S., ... Vitart, F. (2011). The era-interim reanalysis: configuration and performance of the data assimilation system. *Quarterly Journal of the Royal Meteorological Society*, *137*(656), 553-597. doi: 10.1002/qj.828

Espinoza, J. C., Ronchail, J., Lengaigne, M., Quispe, N., Silva, Y., Bettolli, M. L., ... Llacza, A. (2013, Oct 01). Revisiting wintertime cold air intrusions at the east of the andes: propagating features from subtropical argentina to peruvian amazon and relationship with large-scale circulation patterns. *Climate Dynamics*, *41*(7), 1983–2002.

Franzke, C. L. E., Jelic, D., Lee, S., & Feldstein, S. B. (2019). Systematic decomposition of the mjo and its northern hemispheric extratropical response into rossby and inertio-gravity components. *Quarterly Journal of the Royal Meteorological Society*, *145*(720), 1147-1164. doi: 10.1002/qj.3484

Garreaud, R. D. (2000). Cold air incursions over subtropical south america: Mean structure and dynamics. *Monthly Weather Review*, *128*(7), 2544-2559. doi: 10.1175/1520-0493(2000)128⟨2544:CAIOSS⟩2.0.CO;2

Garreaud, R. D., & Wallace, J. M. (1998). Summertime incursions of midlatitude air into subtropical and tropical south america. *Monthly Weather Review*, *126*(10), 2713-2733. doi: 10.1175/1520-0493(1998)126⟨2713:SIOMAI⟩2.0.CO;2

Gelbrecht, M., Boers, N., & Kurths, J. (2018). Phase coherence between precipitation in south america and rossby waves. *Science Advances*, *4*(12). doi: 10.1126/sciadv.aau3191

Gonzalez, P. L. M., & Vera, C. S. (2014, Oct 01). Summer precipitation variability over south america on long and short intraseasonal timescales. *Climate Dy-*

namics, *43*(7), 1993–2007. doi: 10.1007/s00382-013-2023-2

Grimm, A. M., & Silva Dias, P. L. (1995). Analysis of tropical-extratropical interactions with influence functions of a barotropic model. *Journal of the Atmospheric Sciences*, *52*(20), 3538-3555. doi: 10.1175/1520-0469(1995)052⟨3538:AOTIWI⟩2.0.CO;2

Hendon, H. H., & Liebmann, B. (1994). Organization of convection within the Madden-Julian oscillation. *J. Geophys. Res.*, *99*(D4), 8073–8083.

Jin, F., & Hoskins, B. J. (1995). The direct response to tropical heating in a baroclinic atmosphere. *Journal of the Atmospheric Sciences*, *52*(3), 307-319. doi: 10.1175/1520-0469(1995)052⟨0307:TDRTTH⟩2.0.CO;2

Jones, C., & Carvalho, L. M. V. (2002). Active and break phases in the south american monsoon system. *Journal of Climate*, *15*(8), 905-914. doi: 10.1175/1520-0442(2002)015⟨0905:AABPIT⟩2.0.CO;2

Kasahara, A. (1980). Effect of zonal flows on the free oscillations of a barotropic atmosphere. *Journal of the Atmospheric Sciences*, *37*(5), 917-929. doi: 10.1175/1520-0469(1980)037⟨0917:EOZFOT⟩2.0.CO;2

Kasahara, A., & Puri, K. (1981). Spectral representation of three-dimensional global data by expansion in normal mode functions. *Monthly Weather Review*, *109*(1), 37-51.

Kikuchi, K., Wang, B., & Kajikawa, Y. (2012). Bimodal representation of the tropical intraseasonal oscillation. *Clim. Dyn.*, *10*, 1989–2000.

Kiladis, G. N., Dias, J., Straub, K. H., Wheeler, M. C., Tulich, S. N., Kikuchi, K., ... Ventrice, M. J. (2014, 2014/05/29). A comparison of OLR and circulation-based indices for tracking the MJO. *Monthly Weather Review*, *142*(5), 1697–1715. doi: 10.1175/MWR-D-13-00301.1

Kiladis, G. N., Straub, K. H., & Haertel, P. T. (2005, 08). Zonal and Vertical Structure of the Madden–Julian Oscillation. *Journal of the Atmospheric Sciences*, *62*(8), 2790-2809. doi: 10.1175/JAS3520.1

Kiladis, G. N., & Weickmann, K. M. (1992, 2014/05/29). Circulation anomalies associated with tropical convection during northern winter. *Monthly Weather Review*, *120*(9), 1900–1923. doi: 10.1175/1520-0493(1992)120⟨1900:CAAWTC⟩2.0.CO;2

Kitsios, V., O'Kane, T. J., & Žagar, N. (2019, 07). A Reduced-Order Representation of the Madden–Julian Oscillation Based on Reanalyzed Normal Mode Coherences. *Journal of the Atmospheric Sciences*, *76*(8), 2463-2480. doi: 10.1175/JAS-D-18-0197.1

Liebmann, B., Kiladis, G. N., Allured, D., Vera, C. S., Jones, C., Carvalho, L. M. V., ... Gonzales, P. L. M. (2011). Mechanisms associated with large daily rainfall events in northeast brazil. *Journal of Climate*, *24*(2), 376-396. doi: 10.1175/2010JCLI3457.1

Liebmann, B., Kiladis, G. N., Carvalho, L. M. V., Jones, C., Vera, C. S., Bladé, I., & Allured, D. (2009, 2014/05/29). Origin of convectively coupled kelvin waves over south america. *Journal of Climate*, *22*(2), 300–315. doi: 10.1175/2008JCLI2340.1

Liebmann, B., Kiladis, G. N., Marengo, J., Ambrizzi, T., & Glick, J. D. (1999, 2014/05/29). Submonthly convective variability over south america and the south atlantic convergence zone. *Journal of Climate*, *12*(7), 1877–1891. doi: 10.1175/1520-0442(1999)012⟨1877:SCVOSA⟩2.0.CO;2

Liebmann, B., & Smith, C. A. (1996). Description of a complete (interpolated) outgoing long-wave radiation dataset. *Bull. Amer. Meteor. Soc.*, *77*, 1275–1277.

Livezey, R. E., & Chen, W. Y. (1983). Statistical field significance and its determination by Monte Carlo techniques. *Mon. Wea. Rev.*, *111*, 46-59.

Lupo, A. R., Nocera, J. J., Bosart, L. F., Hoffman, E. G., & Knight, D. J. (2001). South american cold surges: Types, composites, and case studies. *Monthly Weather Review*, *129*(5), 1021-1041. doi: 10.1175/1520-0493(2001)129⟨1021:

SACSTC⟩2.0.CO;2

Matthews, A. J. (2012). A multiscale framework for the origin and variability of the south pacific convergence zone. *Quarterly Journal of the Royal Meteorological Society*, *138*(666), 1165-1178. doi: 10.1002/qj.1870

Mayta, V. C., Ambrizzi, T., Espinoza, J. C., & Silva Dias, P. L. (2019). The role of the madden-julian oscillation on the amazon basin intraseasonal rainfall variability. *International Journal of Climatology*, *39*(1), 343-360. doi: 10.1002/joc.5810

Mayta, V. C., Silva, N. P., Ambrizzi, T., Dias, P. L. S., & Espinoza, J. C. (2020). Assessing the skill of all-season diverse Madden–Julian oscillation indices for the intraseasonal Amazon precipitation. *Climate Dynamics*, *54*(7-8), 3729–3749. doi: 10.1007/s00382-020-05202-9

Mo, K. C., & Higgins, R. W. (1998). The pacific–south american modes and tropical convection during the southern hemisphere winter. *Monthly Weather Review*, *126*(6), 1581-1596. doi: 10.1175/1520-0493(1998)126⟨1581:TPSAMA⟩2.0.CO;2

Mori, M., & Watanabe, M. (2008). The growth and triggering mechanisms of the pna: A mjo-pna coherence. *Journal of the Meteorological Society of Japan. Ser. II*, *86*(1), 213-236. doi: 10.2151/jmsj.86.213

Nogués-Paegle, J., & Mo, K. C. (1997). Alternating wet and dry conditions over south america during summer. *Monthly Weather Review*, *125*(2), 279-291. doi: 10.1175/1520-0493(1997)125⟨0279:AWADCO⟩2.0.CO;2

North, G. R., Bell, T. L., Cahalan, R. F., & Moeng, F. J. (1982). Sampling errors in the estimation of empirical orthogonal functions. *Mon. Wea. Rev.*, *110*, 699–706.

Paegle, J. N., Byerle, L. A., & Mo, K. C. (2000). Intraseasonal modulation of south american summer precipitation. *Monthly Weather Review*, *128*(3), 837-850. doi: 10.1175/1520-0493(2000)128⟨0837:IMOSAS⟩2.0.CO;2

Ramirez, E., da Silva Dias, P. L., & Raupp, C. F. M. (2017). Multiscale atmosphere-ocean interactions and the low-frequency variability in the equatorial region. *Journal of the Atmospheric Sciences*, *74*(8), 2503-2523. doi: 10.1175/JAS-D-15-0325.1

Raphaldini, B., Wakate Teruya, A. S., Silva Dias, P. L., C. Mayta, V., & Takara, V. J. (2020). Normal mode perspective on the 2016 qbo disruption: Evidence for a basic state regime transition. *Geophysical Research Letters*, *47*(14), e2020GL087274. doi: 10.1029/2020GL087274

Raupp, C., & Silva Dias, P. (2010). Interaction of equatorial waves through resonance with the diurnal cycle of tropical heating. *Tellus A*, *62*(5).

Raupp, C. F. M., Dias, P. L. S., Tabak, E. G., & Milewski, P. (2008). Resonant wave interactions in the equatorial waveguide. *J. Atmos. Sci*, *65*(11), 3398–3418.

Raupp, C. F. M., & Silva Dias, P. L. (2009, 2014/06/02). Resonant wave interactions in the presence of a diurnally varying heat source. *Journal of the Atmospheric Sciences*, *66*(10), 3165–3183. doi: 10.1175/2009JAS2899.1

Satyamurty, P., Nobre, C. A., & Silva Dias, P. L. (1998). *South America* (D. J. Karoly & D. G. Vincent, Eds.). Boston, MA: American Meteorological Society. doi: 10.1007/978-1-935704-10-25

Silva Dias, P. L., & Bonatti, J. P. (1985). A preliminary study of the observed vertical mode structure of the summer circulation over tropical south america. *Tellus A: Dynamic Meteorology and Oceanography*, *37*(2), 185-195. doi: 10.3402/tellusa.v37i2.11665

Silva Dias, P. L., Schubert, W. H., & DeMaria, M. (1983). Large-scale response of the tropical atmosphere to transient convection. *Journal of the Atmospheric Sciences*, *40*(11), 2689–2707.

Souza, E. B., & Ambrizzi, T. (2006). Modulation of the intraseasonal rainfall over

tropical brazil by the madden-julian oscillation. *International Journal of Climatology*, *26*(13), 1759-1776. doi: 10.1002/joc.1331

Straub, K. H., & Kiladis, G. N. (2002). Observations of a convectively coupled kelvin wave in the eastern pacific itcz. *Journal of the Atmospheric Sciences*, *59*(1), 30–53.

Tanaka, H. (1985). Global energetics analysis by expansion into three-dimensional normal mode functions during the fgge winter. *Journal of the Meteorological Society of Japan. Ser. II*, *63*(2), 180-200. doi: 10.2151/jmsj1965.63.2_180

Vera, C., Higgins, W., Amador, J., Ambrizzi, T., Garreaud, R., Gochis, D., ... Zhang, C. (2006). Toward a unified view of the american monsoon systems. *Journal of Climate*, *19*(20), 4977-5000. doi: 10.1175/JCLI3896.1

Vera, C. S., Alvarez, M. S., Gonzalez, P. L. M., Liebmann, B., & Kiladis, G. N. (2018, Sep 01). Seasonal cycle of precipitation variability in south america on intraseasonal timescales. *Climate Dynamics*, *51*(5), 1991–2001.

Wang, S., Ma, D., Sobel, A. H., & Tippett, M. K. (2018). Propagation characteristics of bsiso indices. *Geophysical Research Letters*, *45*(18), 9934-9943. doi: 10.1029/2018GL078321

Wheeler, M., & Kiladis, G. (1999). Convectively-coupled equatorial waves: Analysis of clouds in the wavenumber-frequency domain. *J. Atmos. Sci.*, *56*, 374–399.

Wheeler, M. C., & Hendon, H. H. (2004). An all-season real-time multivariate MJO index: Development of an index for monitoring and prediction. *Mon. Wea. Rev*, *132*(8), 1917–1932.

Wheeler, M. C., Kiladis, G. N., & Webster, P. J. (2000). Large-scale dynamical fields associated with convectively coupled equatorial waves. *Journal of the Atmospheric Sciences*, *57*(5), 613–640.

Žagar, N., & Franzke, C. L. (2015). Systematic decomposition of the madden-julian oscillation into balanced and inertio-gravity components. *Geophysical Research Letters*, *42*(16), 6829–6835.

Žagar, N., Kasahara, A., Terasaki, K., Tribbia, J., & Tanaka, H. (2015). Normal-mode function representation of global 3-D data sets: open-access software for the atmospheric research community. *Geoscientific Model Development*, *8*(4), 1169–1195. doi: 10.5194/gmd-8-1169-2015

Appendix A Upper-level Regression fields

Figure A1 shows the LFI regression patterns of upper-level winds and velocity potential (CHI). It was constructed in order to show the contribution of the IGW modes (Fig. A1b) in the total fields, mainly during the Oct-Apr season. Indeed, it well-described the wavenumber-1 (k=1) structure associated with eastward MJO propagation into South America.

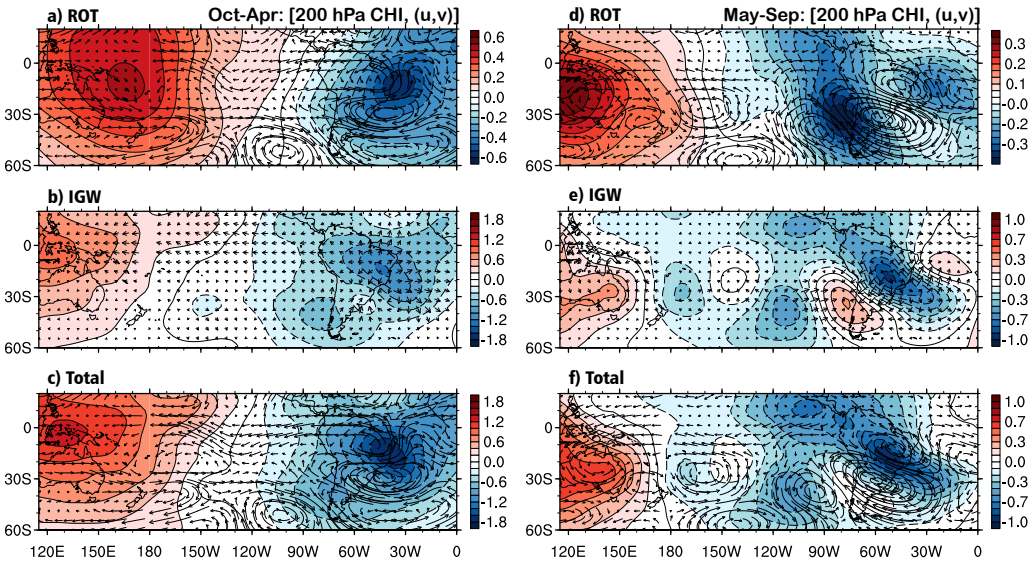

A1. As in Figure 6, but showing upper-level velocity potential (CHI) instead of streamfunction.

Table 1. Low-frequency Intraseasonal (LFI) seasonal cycle and their associated precursors. Dates of the LFI events at day 0 are determined from PC1 of the EOF analysis. Boldface dates indicate that day 0 is observed as an active phase ($Amplitude = (PC1^2 + PC2^2)^{1/2} \geq 1$) in RMM or/and OMI index. In parenthesis are also presented the precursors associated with each event, where T, E, and OP means that LFI events are preceded by tropical, extratropical (HFI), and other precursors, respectively.

Seasonal cycle of the Low-frequency Intraseasonal (LFI) events and their associated precursor					
Year	$Jan-Mar$	$Apr-Jun$	$Jul-Sep$	$Oct-Dec$	Total
1980	-	**04/07 (T)**	07/04 (OP)	-	2
1981	**03/19 (T/E)**	**04/28 (T/E)**; 06/11 (E)	**08/17 (T)**	**10/08 (T/E)**	5
1982	01/11 (T); 03/09 (T)	**04/15(T)**; 06/22 (T)	08/13 (OP)	-	5
1983	**02/01 (T); 03/20 (T/E)**	05/28 (OP)	**09/11 (T)**	-	4
1984	-	06/14 (OP)	-	**10/24 (T)**; 11/30 (OP)	3
1985	**01/20 (T)**; **03/03 (T/E)**	-	09/29 (OP)	12/02 (T); **12/30(T/E)**	5
1986	-	05/07 (T/E)	**07/12 (T); 08/21 (T/E)**	10/09 (T/E); **12/25 (E)**	5
1987	-	**05/01 (T)**	-	10/02 (OP)	2
1988	02/14 (T)	**04/19 (T)**	-	10/08 (T)	3
1989	-	**04/23 (T); 06/17(T)**	-	**12/19 (T)**	3
1990	**02/20 (T)**	**05/09 (T)**	**07/17 (T/E); 08/29 (T)**	**10/24(T); 11/30 (T)**	6
1991	**01/08 (T)**; 03/21 (T)	**05/09 (T); 06/17 (T)**	**09/23 (T)**	**11/11 (T)**	6
1992	**01/27 (T)**	**04/22 (T)**	**07/04 (T); 09/14 (E)**	-	4
1993	**02/18 (T)**	04/01 (T)	**08/15 (T/E)** ; 09/19 (E)	**12/30 (E)**	5
1994	**03/07 (T)**	**05/27 (T)**	09/04 (OP)	**10/14 (T);** 11/23 (OP)	5
1995	02/03(T)	05/13 (OP)	-	10/07 (T)	3
1996	**03/11 (T)**	**05/19 (T); 06/28 (T)**	09/05 (T)	**11/20 (T)**	5
1997	-	**06/05 (T/E)**	08/07 (E); 09/17 (OP)	**12/04 (OP)**	4
1998	**01/16 (T/E)**	-	08/07 (OP)	-	2
1999	**01/05 (OP); 03/04 (T)**	**05/08 (T/E)**	**09/17 (T)**	10/26 (T); **12/27 (T/E)**	6
2000	02/02 (OP)	04/19 (E)	**09/07 (T)**	**11/05 (T); 12/12 (T/E)**	5
2001	-	**05/16 (T)**	**07/22 (T)**	**10/16 (T)**	3
2002	**01/06 (T)**	-	**07/08 (T/E)**; 09/12 (T)	**11/02 (OP)**; **12/14 (T)**	5
2003	-	**06/02 (T)**	-	**11/02 (T)**	2
2004	**01/11 (T/E)**	-	**07/12 (T); 08/19 (T)**	**10/14 (T/E)**	4
2005	-	**04/26 (T/E)**; 06/26 (OP)	**09/27 (T)**	-	3
2006	**02/08 (T)**	**05/23 (T/E)**	-	12/07 (OP)	3
2007	**02/12 (T/E)**	04/20 (T); **05/24 (T/E)**	**07/23 (T)**	**12/02 (T/E)**	5
2008	**01/27 (T)**	**04/05 (T)**; 06/23 (OP)	08/03 (OP); **09/25 (T)**	11/20 (OP)	6
2009	**03/31 (T)**	-	07/22 (OP)	**10/27 (T/E)**; **12/25 (T)**	4
2010	-	**05/29 (T)**	**07/26 (OP)**	-	2
2011	**03/04 (OP)**	-	-	**10/12 (T/E)**	2
2012	03/18 (OP)	-	07/22 (OP)	11/16 (T)	3
2013	**01/22 (T/E)**	04/17 (T); 06/19 (E)	-	12/18 (E)	4
2014	**02/23 (E)**	-	**07/25 (E);** 09/20 (OP)	-	3
2015	**01/31 (T)**	04/28 (T)	**07/06 (T/E);** 08/30 (T)	-	4
2016	**01/14 (T)**	03/27 (T); **06/06 (T)**	08/27 (T)	10/02 (OP); **11/12 (E)**	6